

## RESEARCH ARTICLE

10.1002/2016JB013543

## Key Points:

- We build an integrated thermodynamic model of Fe and Al chemistry for lower mantle conditions
- We find a new stratified picture of the Fe speciation profile with respect to pressures
- The Fe partitioning between ferropericlasite and bridgmanite is dominated by  $\text{Fe}^{2+}$  spin transition

## Supporting Information:

- Supporting Information S1

## Correspondence to:

D. Morgan,  
ddmorgan@wisc.edu

## Citation:

Xu, S., J.-F. Lin, and D. Morgan (2017), Iron partitioning between ferropericlasite and bridgmanite in the Earth's lower mantle, *J. Geophys. Res. Solid Earth*, 122, 1074–1087, doi:10.1002/2016JB013543.

Received 13 SEP 2016

Accepted 5 FEB 2017

Accepted article online 7 FEB 2017

Published online 24 FEB 2017

## Iron partitioning between ferropericlasite and bridgmanite in the Earth's lower mantle

Shenzhen Xu<sup>1</sup> , Jung-Fu Lin<sup>2,3</sup> , and Dane Morgan<sup>1,4</sup> 

<sup>1</sup>Materials Science Program, University of Wisconsin-Madison, Madison, Wisconsin, USA, <sup>2</sup>Department of Geological Sciences, Jackson School of Geoscience, University of Texas at Austin, Austin, Texas, USA, <sup>3</sup>Center for High Pressure Science and Technology Advanced Research, Shanghai, China, <sup>4</sup>Department of Materials Science and Engineering, University of Wisconsin-Madison, Madison, Wisconsin, USA

**Abstract** Earth's lower mantle is generally believed to be seismically and chemically homogeneous because most of the key seismic parameters can be explained using a simplified mineralogical model at expected pressure-temperature conditions. However, recent high-resolution tomographic images have revealed seismic and chemical stratification in the middle-to-lower parts of the lower mantle. Thus far, the mechanism for the compositional stratification and seismic inhomogeneity, especially their relationship with the speciation of iron in the lower mantle, remains poorly understood. We have built a complete and integrated thermodynamic model of iron and aluminum chemistry for lower mantle conditions and from this model has emerged a stratified picture of the valence, spin, and composition profile in the lower mantle. Within this picture the lower mantle has an upper region with  $\text{Fe}^{3+}$ -enriched bridgmanite with high-spin ferropericlasite and metallic Fe and a lower region with low-spin, iron-enriched ferropericlasite coexisting with iron-depleted bridgmanite and almost no metallic Fe. The transition between the regions occurs at a depth of around 1600 km and is driven by the spin transition in ferropericlasite, which significantly changes the iron partitioning and speciation to one that favors  $\text{Fe}^{2+}$  in ferropericlasite and suppresses  $\text{Fe}^{3+}$  and metallic iron formation. These changes lead to lowered bulk sound velocity by 3–4% around the middle-lower mantle and enhanced density by ~1% toward the lowermost mantle. The predicted chemically and seismically stratified lower mantle differs dramatically from the traditional homogeneous model.

## 1. Introduction

Recent mineral physics studies have revealed the complex nature of the spin and valence states of iron in ferropericlasite (Fp) and bridgmanite (Pv) at high pressure and temperature ( $P$ - $T$ ). The spin crossover of  $\text{Fe}^{2+}$  in Fp occurs over a wide  $P$ - $T$  range corresponding to approximately 1100 km to 1900 km in depth [Badro *et al.*, 2003; Goncharov *et al.*, 2006; Lin *et al.*, 2005; Persson *et al.*, 2006; Sturhahn *et al.*, 2005; Tsuchiya *et al.*, 2006; Vilella *et al.*, 2015], whereas the  $\text{Fe}^{3+}$  in the octahedral site (B site) of Pv undergoes the transition from about 1000 km to 1500 km in depth [Catalli *et al.*, 2011a; Hsu *et al.*, 2011, 2012], both depending somewhat on temperature. Of particular interest to our understanding of deep-mantle seismology are the effects of the spin transition on the density and sound velocity profiles in lower mantle Fp [Cammarano *et al.*, 2010; Crowhurst *et al.*, 2008; Marquardt *et al.*, 2009; Wu and Wentzcovitch, 2014], where abnormal velocity softening within the transition has been reported and the full low-spin state has been found to exhibit distinct elastic behaviors from its full high-spin counterpart. Also of interest is the variation of Fe valence states ( $\text{Fe}^{2+}$ ,  $\text{Fe}^{3+}$ , and  $\text{Fe}^0$ ) with respect to depth because this variation determines both the amount of Fe that undergoes each type of spin transition and the amount of metallic Fe ( $\text{Fe}^0$ ), which has a significant influence on our understanding of the partial melting in the mantle [Fukai and Suzuki, 1986] and the Earth's core formation [Halliday and Lee, 1999]. In addition, the Fe partitioning between Pv and Fp ( $K_D^{\text{Pv-Fp}} = (\text{Fe}/\text{Mg})_{\text{Pv}}/(\text{Fe}/\text{Mg})_{\text{Fp}}$ ) is also critical to the interpretation of the deep-Earth geochemistry, because changes in partitioning can lead to a chemically stratified lower mantle that may behave distinctly from a traditional homogeneous model. While all these separate aspects of spin, valence, and partitioning are important, their impact on the lower mantle can only be properly determined when their couplings are taken into account through an integrated picture of Fe chemistry under lower mantle conditions. The Fe chemistry is expected to couple to multiple interacting aspects of the lower mantle environment, including  $P$ - $T$ , spin transitions, oxygen fugacity, and aluminum substitution. Understanding and quantifying such couplings requires an integrated thermodynamic model of Fe chemistry that incorporates all of these environmental factors.

Using a pyrolitic composition, iron has been shown experimentally to partition into Pv and Fp with a  $K_D^{\text{Pv-Fp}} \approx 0.5$  ( $K_D^{\text{Pv-Fp}}$  is defined as  $[\text{Fe}^{2+} + \text{Fe}^{3+}]_{\text{Pv}} / ([\text{Mg}^{2+}]_{\text{Pv}}) / ([\text{Fe}^{2+}]_{\text{Fp}} / [\text{Mg}^{2+}]_{\text{Fp}})$ ) [Irifune *et al.*, 2010; Nakajima *et al.*, 2012]. However,  $K_D^{\text{Pv-Fp}}$  was observed to significantly increase to almost 0.9 at approximately 28 GPa (or ~750 km depth) [Irifune *et al.*, 2010]. The change in  $K_D^{\text{Pv-Fp}}$  has been attributed to the formation of  $\text{Fe}^{3+}$ -rich Pv promoted by the charge-coupled substitution of  $\text{Al}^{3+}$  and  $\text{Fe}^{3+}$  [Frost *et al.*, 2004; Irifune *et al.*, 2010]. On the other hand, self-disproportionation of  $\text{Fe}^{2+}$  into  $\text{Fe}^0$  and  $\text{Fe}^{3+}$  has also been used to explain the observations of the high  $\text{Fe}^{3+}$  content in Pv and the coexistence of metallic iron [Frost *et al.*, 2004]. At  $P$ - $T$  conditions below the middle-lower mantle, experimental studies have also shown that  $K_D^{\text{Pv-Fp}}$  decreases to approximately 0.5 in the pyrolitic composition or to 0.2 in the olivine composition [Auzende *et al.*, 2008; Irifune, 1994; Irifune *et al.*, 2010; Kesson *et al.*, 1998; Kobayashi *et al.*, 2005; Sakai *et al.*, 2009; Sinmyo *et al.*, 2008a; Wood, 2000]. A recent theoretical work of Muir and Brodholt [2016] studied the ferrous iron partitioning between Pv and Fp and predicted that  $\text{Fe}^{2+}$  prefers Fp rather than Pv. Their calculations showed a convex shape feature of the  $K_D^{\text{Pv-Fp}}(P)$  profile with a peak ( $K_D^{\text{Pv-Fp}} \sim 0.25$ ) at 50 GPa and gradually decreasing to 0.05 at higher pressures. However, they only calculated the ferrous iron  $\text{Fe}^{2+}$  partitioning in the two phases, which is  $(\text{Mg}_{1-x}\text{Fe}^{2+}_x)\text{O} + \text{MgSiO}_3 \rightleftharpoons (\text{Mg}_{1-y}\text{Fe}^{2+}_y)\text{SiO}_3 + \text{MgO}$ . The important impurity species  $\text{Al}^{3+}$  and  $\text{Fe}^{3+}$  in the Pv phase, the possible formation of metallic Fe phase, and the influence of the surrounding oxygen fugacity ( $f\text{O}_2$ ) conditions are not considered in their thermodynamic model. Thus far, the relationship of Fe partitioning with Fe valence and spin states at lower mantle relevant  $P$ - $T$ , composition ( $X$ ), and  $f\text{O}_2$  conditions remain largely unexplored. Here we have developed an integrated and validated ab initio and empirical fitting-based thermodynamic model to explicitly predict the partitioning behavior of Fe in lower mantle Pv and Fp over a wide range of likely  $P$ - $T$ - $X$ - $f\text{O}_2$  conditions in pyrolite and olivine compositional models. We have used density functional theory (DFT) calculations with the HSE06 hybrid exchange-correlation functional [Heyd *et al.*, 2003] for the relevant enthalpies. The equilibrium iron valence, spin states, and occupation in the sublattices of Fp and Pv are determined by minimizing the total Gibbs free energy of the system (section 4.2 for details). Since it is well known that the variation in the oxygen fugacity ( $f\text{O}_2$ ) affects Fe valence states in the upper mantle minerals, it is important to consider its possible impact on the lower mantle bridgmanite, and therefore, here we have considered two different scenarios in our modeling: a closed system with no exchange of free oxygen with surrounding materials where  $\text{Fe}^{3+}$  is produced through the charge disproportionation (chg. disp.) reaction ( $3\text{Fe}^{2+} \rightarrow 2\text{Fe}^{3+} + \text{Fe}^0$ ) [Frost *et al.*, 2004; Xu *et al.*, 2015; Zhang and Oganov, 2006] and an open system with free oxygen buffered through oxygen exchange with surrounding materials in the system (section 4.2 for details). These modeling approaches allow us to investigate the iron chemistry under lower mantle conditions (closed system scenario) and to compare with experimental observations where the  $f\text{O}_2$  is usually buffered by certain capsules (open system scenario), typically resulting in relatively oxidizing conditions compared to the lower mantle [Irifune *et al.*, 2010]. The effects of  $\text{Al}^{3+}$  incorporation are investigated via the integration of the  $\text{Al}^{3+}$  substitution energetics in the pyrolite system, and comparison with the olivine system yields understanding of the discrepancy between Al-bearing and Al-free systems of the reported  $K_D$  values in previous experimental reports [Auzende *et al.*, 2008; Irifune, 1994; Irifune *et al.*, 2010; Kesson *et al.*, 1998; Kobayashi *et al.*, 2005; Sakai *et al.*, 2009; Sinmyo *et al.*, 2008a; Wood, 2000].

## 2. Results and Discussion

Our ab initio and empirical fitting-based thermodynamic model predicts that a gradual spin transition occurs for  $\text{Fe}^{2+}$  in Fp from approximately 40 GPa to 80 GPa and for B-site  $\text{Fe}^{3+}$  in Pv from approximately 30 GPa to 50 GPa (Figure 1a), both of which are along an expected geotherm [Brown and Shankland, 1981]. The predicted fractions of different Fe species in the pyrolitic compositional system show that high-spin  $\text{Fe}^{2+}$  is the predominant form of Fe in Fp and Pv around the top of the lower mantle and it should be noted that  $\text{Fe}^{3+}$  is produced only through the chg. disp. reaction in Pv. Our model predicts the formation of metallic Fe from the top to the middle-lower mantle. Once sufficient  $\text{Al}^{3+}$  is dissolved into Pv, most B-site  $\text{Fe}^{3+}$  is driven to the A-site (Figure 1b) (details of the Al content in Pv are discussed in section 4.1, and the driving force for A-site occupancy is discussed in supporting information (SI) section 2). The loss of B-site  $\text{Fe}^{3+}$  implies that the spin transition of Pv B-site  $\text{Fe}^{3+}$  will not have a significant impact on the physical and chemical properties of the lower mantle [Hsu *et al.*, 2012]. Furthermore,  $\text{Fe}^{2+}$  preferentially partitions into Fp across its spin transition such that Pv is depleted of iron toward the lowermost mantle. This spin-induced iron partitioning

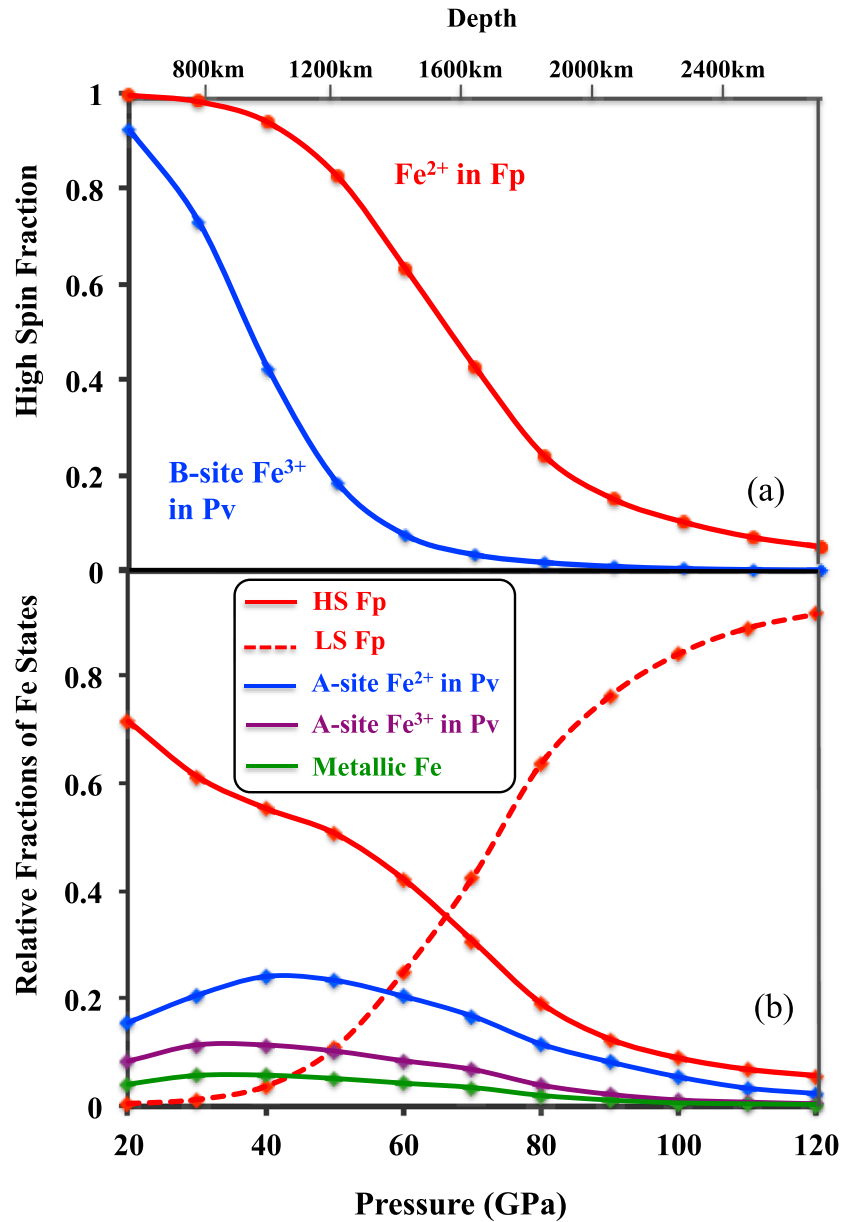


**Figure 1.** Spin and valence states of iron and their relative fractions in the lower mantle ferropericlase (Fp) and bridgmanite (Pv) along an expected geotherm [Brown and Shankland, 1981]. Solid symbols represent our theoretically predicted results, while colored lines are fitted to the data to show trends. (a) Fractions of the high-spin  $\text{Fe}^{2+}$  in Fp and high-spin B-site  $\text{Fe}^{3+}$  in Pv are plotted as red and blue lines, respectively. (b) Relative fractions of iron in lower mantle Fp, Pv, and metallic iron with respect to the total amount of Fe in a pyrolitic compositional model. The B-site  $\text{Fe}^{3+}$  content in Pv is significantly smaller ( $\leq 10^{-6}$  mol fraction of Fe) than the contents of other Fe species and is not shown for clarity.

suppresses the aforementioned chg. disp. reaction, significantly decreasing the presence of the metallic iron in the lower parts of the lower mantle. Therefore, the formation of metallic Fe is predicted to occur only from the top to the middle-lower mantle.

The partitioning coefficient ( $K_D^{\text{Pv-Fp}}$ ) is calculated using the predicted iron contents in Fp and Pv for expected geotherm  $P$ - $T$  conditions of the pyrolitic lower mantle (Figure 2a, and  $\ln(K_D^{\text{Pv-Fp}})$  is given in SI Figure S6). Our predicted  $K_D$  curve shows a convex shape starting with an initial value of 0.2 at 22 GPa, a peak value of 0.34 at 40 GPa, and a continuous decrease between 40 GPa and 120 GPa reaching a minimum value of almost zero. At the topmost lower mantle,  $\text{Fe}^{2+}$  is more energetically favorable to partition into Fp. As the  $P$ - $T$  increases up

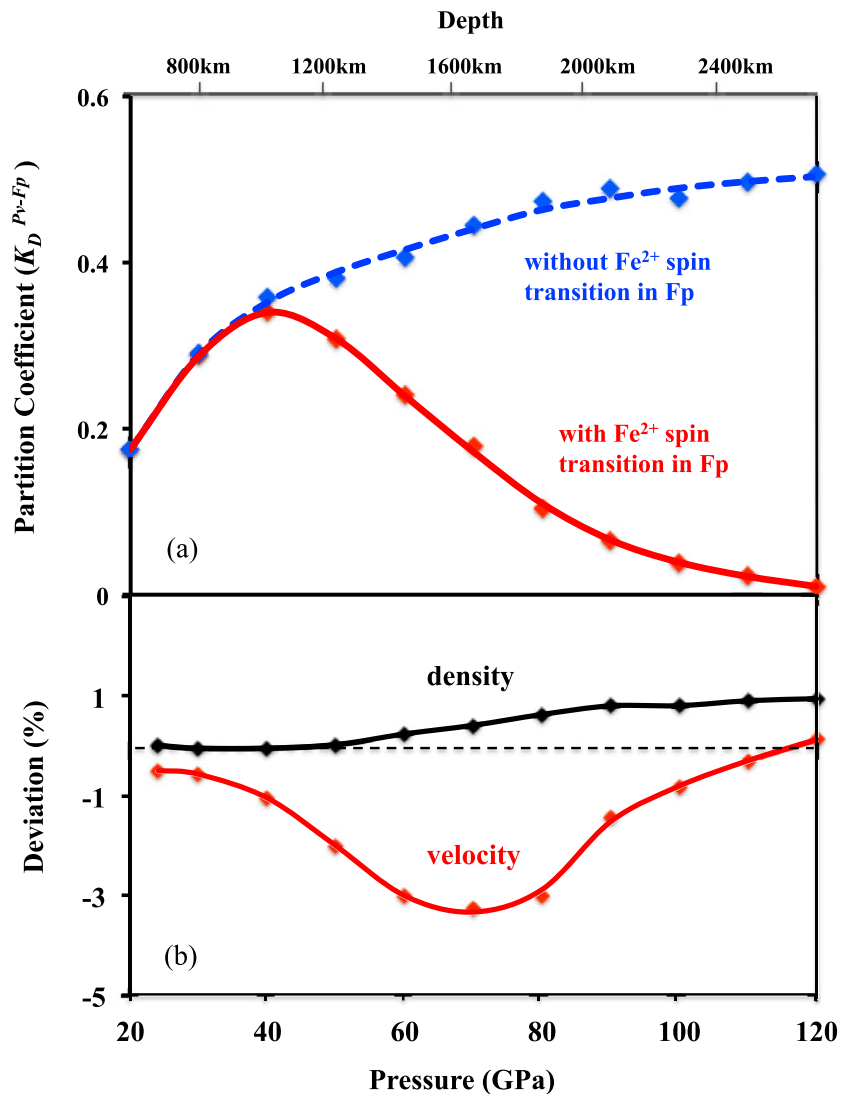


**Figure 2.** Partition coefficient ( $K_D^{Pv-Fp}$ ) of iron and deviations in the density and bulk sound velocity due to the Fp  $Fe^{2+}$  spin transition in a pyrolytic lower mantle composition along an expected geotherm [Brown and Shankland, 1981]. (a) Red data points with fitted solid curve are the  $K_D$  considering the spin transition  $Fe^{2+}$  in Fp. Blue data points with fitted dashed line curve are the  $K_D$  without the influence of this spin transition;  $K_D$  values continue to increase with increasing pressure along the geotherm. (b) The deviation is defined as  $(X' - X_{ref})/X_{ref}$ , where  $X'$  is the physical property (density ( $\rho$ ) or bulk sound velocity ( $V_\phi$ )) calculated using a pyrolytic model across the Fe spin transition along an expected geotherm [Brown and Shankland, 1981],  $X_{ref}$  is the reference value without the spin transition. Black and red data points and fitted solid curves correspond to the density and bulk sound velocity deviations (%), respectively, from the reference profiles without the spin transition of  $Fe^{2+}$  in Fp.

to 40 GPa, the incorporation of  $Al^{3+}$  into Pv through the dissolution of majorite drives both high-spin  $Fe^{2+}$  and  $Fe^{3+}$  into the A-site of the Pv lattice. Another reason causing more iron partitioning into Pv from 20 to 40 GPa is that the majority of Fp  $Fe^{2+}$  is in the high-spin state, where its enthalpy becomes relatively higher as pressure increases as compared to Pv  $Fe^{2+}$  (see SI section 2.3 for detailed discussion). Compared with the  $K_D$  curve without the spin transition in Fp that continuously increases with increasing pressure (Figure 2a), it is evident that the dramatic decrease in the  $K_D$  curve starting at approximately 40 GPa is caused by the spin transition in Fp. The volume collapse and the associated reduction in the Gibbs free energy make the low-spin  $Fe^{2+}$  with a smaller volume more energetically favorable in Fp, as opposed to staying in Pv. As the spin crossover continues to occur with increasing depth, the  $K_D$  value below the spin transition zone reaches almost zero, and the majority of the iron partitions into Fp at the lowermost mantle. This

partitioning also destabilizes metallic iron in the system, reducing it to less than 1% of the Fe toward the deeper lower mantle. The Fp  $\text{Fe}^{2+}$  spin transition governing Fe partitioning profile shown in our calculation matches very well with the results in the recent theoretical work of *Muir and Brodholt* [2016]. The same convex shape feature of the Fe partitioning coefficient with respect to pressures was reported in their work [*Muir and Brodholt*, 2016, Figure 7]. The peak position was 50 GPa in their calculation, very close to the 40 GPa peak position in our results (Figure 2a). For the quantitative comparison, the peak value of Fe partitioning coefficient was about 0.25 in their results, while we find a peak value about 0.35 in our calculation. This small quantitative difference may come from the fact that Muir and Brodholt did not include the  $\text{Fe}^{3+}$  and  $\text{Al}^{3+}$  in the Pv phase in their model. As the existence of  $\text{Fe}^{3+}$  and  $\text{Al}^{3+}$  increases the Fe content in the Pv phase, their inclusion in our model is expected to yield a relatively higher Fe partitioning coefficient  $K_D^{\text{Pv-Fp}}$ . In addition, Muir and Brodholt based their DFT calculations on the generalized gradient approximation with the Hubbard U corrections (GGA + U) while we used the HSE06 hybrid functional in our work, which is generally believed to be a more consistent and accurate method. However, our results are consistent with their findings both qualitatively and quantitatively, lending support to both models.

To understand the consequences of Fp  $\text{Fe}^{2+}$  spin transition and Fe partitioning on the seismic profiles of the Earth's lower mantle, we have also modeled the mass density ( $\rho$ ) and bulk sound velocity ( $V_\phi$ ) profiles of a representative pyrolitic lower mantle composition along an expected mantle geotherm [*Brown and Shankland*, 1981] (calculation details are shown in SI section 4.2 [*Tange et al.*, 2012, 2009; *Dubrovinsky et al.*, 2000; *Lu et al.*, 2013; *Murakami et al.*, 2012; *Ricolleau et al.*, 2010; *Shukla et al.*, 2015; *van Westrenen et al.*, 2005; *Wang et al.*, 2015; *Wu and Wentzcovitch*, 2014]) and compared them with the density and bulk velocity without the  $\text{Fe}^{2+}$  spin transition in Fp (Figure 2b). Here the bulk sound velocity is defined as  $V_\phi = (K_S/\rho)^{1/2}$ , where  $K_S$  is the adiabatic bulk modulus and values are taken along the geotherm. We only include Pv, Fp, and metallic Fe in our model as they occupy more than 90% of the volume of the lower mantle (SI section 4.2). The starting zero-pressure relative volumetric ratio of Pv over Fp in our pyrolitic model is  $V(\text{Al, Fe-bearing Pv}):V(\text{Fp}) = 3.5:1$  [*Irifune et al.*, 2010]. Our calculated density and velocity profiles display continuous increase with increasing depth without any abrupt changes. However, compared with the calculated profiles without the spin transition, we do notice lowered bulk sound velocity around middle-lower mantle by 3–4% and enhanced density by 1% toward the bottom of the lower mantle. These changes can be explained by the spin transition of  $\text{Fe}^{2+}$  in Fp. As the low-spin  $\text{Fe}^{2+}$  in Fp has a relatively smaller volume than its high-spin counterpart, the volume of Fp will decrease when the spin transition occurs, increasing the density of the system near the bottom of the lower mantle. This volume collapse also causes a softened bulk modulus in the spin transition region (40–80 GPa) leading to a lowered bulk sound velocity ( $V_\phi = (K_S/\rho)^{1/2}$ ) for the system due to the spin transition. The predicted profiles also show a lowered bulk sound velocity by up to 2% with respect to the preliminary reference Earth model (see SI section 3.4 [*Dziewonski and Anderson*, 1981]).

Comparison of our theoretical predictions in the oxidation reaction model at experimental  $P$ - $T$ - $f\text{O}_2$  conditions with previous experimental results [*Auzende et al.*, 2008; *Irifune*, 1994; *Irifune et al.*, 2010; *Kesson et al.*, 1998; *Kobayashi et al.*, 2005; *Sakai et al.*, 2009; *Sinmyo et al.*, 2008a; *Wood*, 2000] for the iron partitioning shows distinctions between the pyrolite composition containing  $\text{Al}^{3+}$  and the olivine bulk composition without  $\text{Al}^{3+}$ . We use a representative  $f\text{O}_2$  range of  $\log f\text{O}_2[\text{diamond-carbonate}] \leq \log f\text{O}_2 \leq \log f\text{O}_2[\text{diamond-carbonate}] + 2$ , as discussed in SI section 3.2 [*Irifune et al.*, 2010; *Pownceby and O'Neil*, 1994; *Stagno and Frost*, 2010; *Stagno et al.*, 2015]. Here the symbol  $f\text{O}_2[X]$  represents the fugacity of material  $X$  under the given  $P$ - $T$  conditions. For the notation of  $f\text{O}_2[\text{diamond-carbonate}]$ , diamond-carbonate represents the equilibrium described by the reaction  $\text{C (diamond)} + \text{O}^{2-} (\text{mineral/melt}) + \text{O}_2 \rightleftharpoons \text{CO}_3^{2-} (\text{mineral/melt})$  [*Stagno and Frost*, 2010]. The equilibrium of carbon (diamond) coexisting with carbonates happens in the (lower mantle relevant) high-pressure condition. The above reaction sets the  $f\text{O}_2$  of the diamond capsule. We assume that within the lower mantle relevant  $P$ - $T$  of our thermodynamic model, the  $f\text{O}_2[\text{diamond-carbonate}]$  is always 4 orders of magnitude lower than the Re-ReO<sub>2</sub> capsule  $f\text{O}_2$  [*Nakajima et al.*, 2012; *Pownceby and O'Neil*, 1994; *Stagno and Frost*, 2010; *Xu et al.*, 2015]. The Re-ReO<sub>2</sub> capsule  $f\text{O}_2$  values as a function of  $P$ - $T$  are explicitly shown in our previous work [*Xu et al.*, 2015]. Although both of the pyrolitic composition curve and the olivine composition curve show convex  $K_D$  behavior with respect to depth, the magnitude of the  $K_D$  in the olivine model is a smaller by a factor of 3–4 than that in the pyrolite model (Figure 3). Under the  $f\text{O}_2$  range studied no chg. disp. occurs and more  $\text{Fe}^{3+}$  is formed and incorporated into Pv compared to under lower mantle  $f\text{O}_2$ , leading to

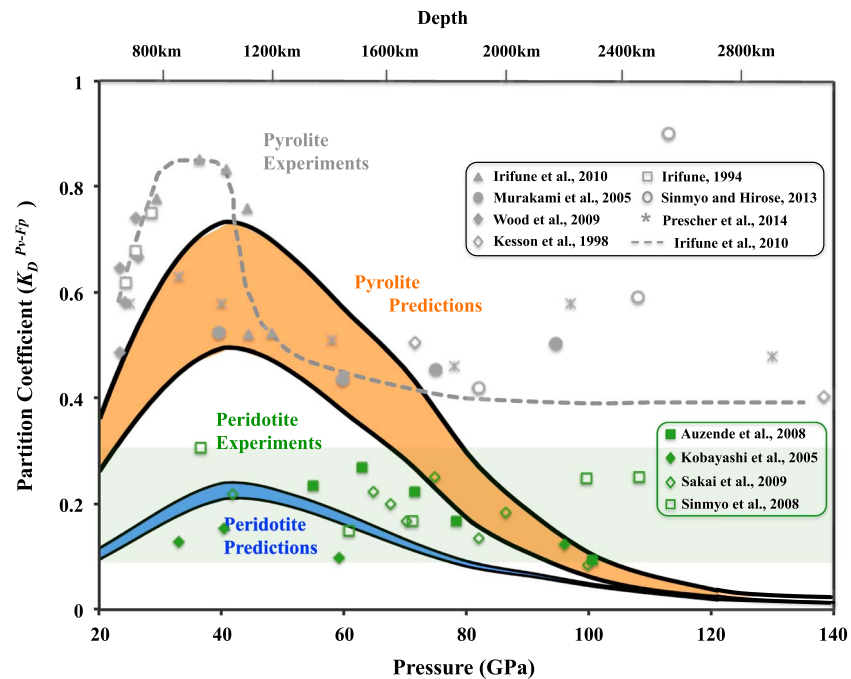


**Figure 3.** Comparison of the partition coefficient ( $K_D$ ) of iron between Pv and Fp from experimental and theoretical results. The orange color region represents our theoretical predicted range of  $K_D$  in a pyrolite composition model. The lower limit (black line) of the orange region corresponds to the condition that  $\log fO_2 = \log fO_2[\text{diamond-carbonate}]$ , and the upper limit (black line) corresponds to the condition that  $\log fO_2 = \log fO_2[\text{diamond-carbonate}] + 2$ . The blue color region represents our predicted  $K_D$  range having a bulk composition of olivine (does not contain any  $Al^{3+}$ ) under the same  $fO_2$  range used in for the pyrolite composition. Experimental  $K_D$  values in a pyrolite composition model (grey symbols) [Irifune, 1994; Irifune et al., 2010; Kesson et al., 1998; Murakami et al., 2005; Prescher et al., 2014; Sinmyo and Hirose, 2013; Wood, 2000] (dashed grey curve is obtained from Irifune et al. [2010]) and olivine composition (green symbols) [Auzende et al., 2008; Kobayashi et al., 2005; Sakai et al., 2009; Sinmyo et al., 2008a] are also plotted for comparison.

a higher  $K_D$  than the chg. disp. reaction model. The contents of different Fe species (valence and spin states) in the pyrolitic compositional model under the  $fO_2[\text{diamond-carbonate}]$  condition are shown in SI section 3.3 Figure S7. This  $fO_2$  effect explains why the pyrolitic  $K_D$  profile in Figure 3 (oxidation reaction model) is higher than that in Figure 2a (chg. disp. reaction) and demonstrates the importance of maintaining realistic lower mantle  $fO_2$  when measuring  $K_D$ . The difference in the magnitude between the pyrolite and olivine compositional models can be explained by the existence of  $Al^{3+}$ , which enhances the  $Fe^{3+}$  content in Pv in the pyrolite model due to the formation of the stable  $Fe^{3+}-Al^{3+}$  pair. As there is no  $Al^{3+}$  in the olivine model, the  $K_D$  values are predicted to remain at 0.1–0.2. For the pyrolite composition, the  $K_D$  profiles from experiments [Irifune, 1994; Irifune et al., 2010; Kesson et al., 1998; Murakami et al., 2005; Wood, 2000] and our simulations both exhibit a convex shape. However, the experimental results show a sharp decrease at approximately 40 GPa and a flattening  $K_D$  value of around 0.5 at higher pressures, which differ from our predicted gradual decrease of  $K_D$  (Figures 2a and 3). The gradual decrease in our calculated  $K_D$  values is due to the broad spin crossover of Fp  $Fe^{2+}$  at high  $P$ - $T$  conditions of the lower mantle [Crowhurst et al., 2008; Lin et al., 2005; Tsuchiya et al., 2006]. Future high  $P$ - $T$  experimental data with lower uncertainties are needed to explain the discrepancies (see SI section 3.3 for further discussion of the discrepancies [Ammann et al., 2010; Irifune, 1994; Irifune et al., 2010; Murakami et al., 2005; Xu et al., 2015]).

Recent two experimental works about the Fe partitioning behavior in a pyrolitic compositional sample under lower mantle relevant  $P$ - $T$  condition showed a large  $K_D$  increase at about 100 GPa [Prescher et al., 2014; Sinmyo and Hirose, 2013]. The explanation proposed in the work [Prescher et al., 2014] for the  $K_D$  increase is that the  $Fe^{2+}$  undergoes a spin transition from the intermediate spin (IS) to the low-spin state in Pv, which is inconsistent with the widely held belief that  $Fe^{2+}$  is always in the HS state in Pv throughout the lower mantle pressure range [Bengtson et al., 2008; Grocholski et al., 2009; Hsu et al., 2010a; Jackson et al., 2005; Lin et al., 2012;



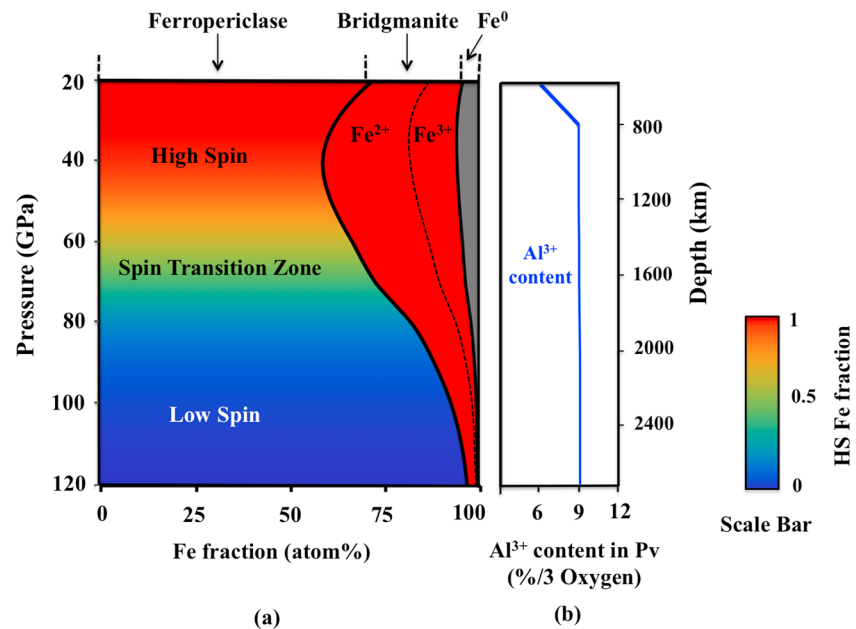


**Figure 4.** Variations of iron chemistry in a pyrolitic lower mantle model. (a) The fractions of the total amount of Fe in atom % in Fp, Pv, and metallic Fe phase ( $\text{Fe}^0$ ) as a function of depth are represented by different color regions. The color gradient represents the high-spin (HS) fraction of iron in both Fp and Pv phases as shown in the vertical bar on the right. In the Pv region, the dashed line separates the A-site  $\text{Fe}^{3+}$  fraction and A-site  $\text{Fe}^{2+}$  fraction in Pv. (b) The Al content in Pv (per three oxygen atoms) is shown by the blue solid line.

Stackhouse *et al.*, 2007]. Moreover, even if we assume that this spin transition occurs, the same  $K_D$  increase behavior would then be expected to happen for the Al-free case as well. However, many previous experimental works failed to observe this abnormally high  $K_D$  around 100 GPa [Auzende *et al.*, 2008; Nakajima *et al.*, 2012; Sakai *et al.*, 2009]. The explanation for this  $K_D$  increase proposed in the work [Sinmyo and Hirose, 2013] is the B-site  $\text{Fe}^{3+}$  spin transition in Pv. However, we would argue that this is unlikely to be the mechanism causing the  $K_D$  increase, because the population of  $\text{Fe}^{3+}$  in B-site in the Al-bearing Pv is very small [Hsu *et al.*, 2012; Zhang and Oganov, 2006] (also discussed in SI section 2.1 in our work) and this spin transition region reported in many previous works is from the upper to the middle-lower mantle [Catalli *et al.*, 2010; Hsu *et al.*, 2011; Lin *et al.*, 2012; Xu *et al.*, 2015]. Specifically, the experimental work of Lin *et al.* [2012] reported that the B-site  $\text{Fe}^{3+}$  spin transition is at about 25 GPa based on their quadrupole splitting (QS) measurement. The simulation work of Hsu *et al.* [2011] predicted that the gradual B-site  $\text{Fe}^{3+}$  spin transition is from 40 GPa to 70 GPa at  $T=2000$  K. So it is less likely for this B-site  $\text{Fe}^{3+}$  spin transition to have such a significant impact on Fe partitioning above 100 GPa. Moreover, some previous experimental works also showed that there is no  $K_D$  increase around or above 100 GPa [Irifune *et al.*, 2010; Kesson *et al.*, 1998]. Even in the paper Prescher *et al.* [2014], they showed that  $K_D$  drops back to 0.5 at about 130 GPa. If this abnormal  $K_D$  increase is indeed caused by the B-site  $\text{Fe}^{3+}$  spin transition,  $K_D$  would stay at the high value down to the bottom of the lower mantle, which is inconsistent with the observation of Prescher *et al.* [2014]. We also note that the explanations for the abnormal  $K_D$  increase in the experimental works Prescher *et al.* [2014] and Sinmyo and Hirose [2013] are inconsistent with each other. Overall, the collected experimental results and efforts to explain them show that there is still significant uncertainty for the experimental  $K_D$  at high pressure ( $>100$  GPa). More work is needed to robustly determine  $K_D$  under these extreme conditions.

### 3. Conclusions

Our calculations have demonstrated that the Earth's lower mantle can be separated into distinct layers that are controlled by the spin crossover in Fp and the  $\text{Al}^{3+}$  substitution in Pv (summarized in Figure 4). The top layer is characterized by  $\text{Fe}^{3+}$ -enriched Pv coexisting with high-spin Fp and metallic iron, while the bottom

layer at depths approximately below about 2000 km exhibits Fe predominantly in Fp and almost no metallic Fe. The transition between the two layers occurs through the Fp  $\text{Fe}^{2+}$  spin transition zone (Figure 4). The volume collapse of Fp caused by the spin crossover also leads to a lowered bulk sound velocity around the middle-lower mantle (Figure 2b). These changes suggest that there is significant iron chemistry-induced stratification of the lower mantle, in contrast to the traditional view of chemical and seismic homogeneity in the lower mantle.

## 4. Methods

### 4.1. Composition Models of Our Thermodynamic System

#### 4.1.1. Pyrolitic Lower Mantle Composition

The Earth's lower mantle is proposed to consist of pyrolite which contains approximately one third basalt and two third peridotite [Ringwood, 1966]. In the pyrolitic compositional model, the mineralogy of the lower mantle is mainly made of approximately 70% bridgmanite ((Mg,Fe)(Si,Al) $\text{O}_3$ ; Pv), 20% ferropericlase ((Mg,Fe)O; Fp), and 10% calcium silicate perovskite ( $\text{CaSiO}_3$ ; Ca-Pv) [Irifune *et al.*, 2010], where all percentages are by volume. Since Ca-Pv likely does not incorporate significant Fe in its lattice, we have only considered Pv and Fp phases in the lower mantle system with a molar ratio [(Mg,Fe)(Si,Al) $\text{O}_3$ ]: [(Mg,Fe)O] = 1: 0.65 corresponding to the volumetric ratio  $V[(\text{Mg,Fe})(\text{Si,Al})\text{O}_3]: V[(\text{Mg,Fe})\text{O}] = 3.5: 1$ . The  $\text{Al}^{3+}$  cation is considered to be mainly incorporated into Pv in the lower mantle. Previous studies have shown that the  $\text{Al}^{3+}$  content in Pv increases with increasing depth at the topmost lower mantle as a result of majorite dissolution into Pv [Irifune, 1994; Irifune *et al.*, 2010]. The depth-dependent  $\text{Al}^{3+}$  content in Pv has been considered in our calculations in order to understand its incorporation mechanism and effects on the iron partitioning between Pv and Fp phases. As the starting composition of the pyrolite system in our calculations,  $\text{Al}^{3+}$  content in Pv increases from 0.06 to 0.09 per three oxygen atoms from 20 GPa to 30 GPa and stays at 0.09 per three oxygen atoms from 30 GPa to 120 GPa, and Fe content is 0.1 per three oxygen atoms in Pv and 0.12 per oxygen atom in Fp from 20 GPa to 120 GPa. The values are based on experimental measurements of Al and Fe content from the previous reference [Irifune *et al.*, 2010].

#### 4.1.2. Olivine Compositional Model

In the olivine compositional model we treat the composition as equal to that of olivine. Olivine, the most abundant mineral in the upper mantle, transforms to Pv and Fp in the lower mantle  $P$ - $T$  conditions. The Fe partitioning coefficient ( $K_D$ ) between Pv and Fp phases with a bulk olivine composition in the lower mantle is also considered in our calculations. Since this system contains a negligible amount of  $\text{Al}^{3+}$ , it is also used to understand how the substitution of  $\text{Al}^{3+}$  in Pv affects the iron partitioning compared to pyrolitic composition case. The typical Fe content in olivine is about 0.1 Fe per Mg-site [Auzende *et al.*, 2008; Sinmyo *et al.*, 2008b]. For the starting composition of the olivine system in our calculation, we have used San Carlos olivine with a representative chemical formula  $(\text{Mg}_{0.9}\text{Fe}_{0.1})_2\text{SiO}_4$ .

### 4.2. Thermodynamic Modeling of the Pv + Fp System

To understand the Fe partitioning the lower mantle under relevant experimental conditions, we have modeled a bulk composition of both pyrolite and olivine, as described in sections 4.1.1 and 4.1.2. In the model, the total amount of iron is fixed throughout all lower mantle conditions. Although the thermodynamic equilibrium state depends on overall stoichiometry and chemical potentials, the equilibrium state is independent of how we approach it. However, for clarity we consider the system to be equilibrating from an initial state with specific spin and site occupancies consistent with the overall stoichiometric constraints. We take our initial state as high-spin (HS)  $\text{Fe}^{2+}$  in both Pv and Fp, in which the HS  $\text{Fe}^{2+}$  occupies the A site in Pv and substitutes for the Mg ions in Fp at the relevant  $P$ - $T$  of the lower mantle [Bengtson *et al.*, 2008; Grocholski *et al.*, 2009; Zhang and Oganov, 2006]. We also assume that  $\text{Al}^{3+}$  enters into the Pv lattice through the charge-coupled substitution in which  $\text{Al}^{3+}$ - $\text{Al}^{3+}$  occupy the A site and B site jointly [Brodholt, 2000]. These initial states are allowed to vary in our calculations in order to reach thermodynamic equilibrium, in which variations are considered for Fe HS and LS states, Fe occupancy of A and B sites in Pv,  $\text{Fe}^{2+}$ , and  $\text{Fe}^{3+}$  valence states, and partitioning of Fe between Fp and Pv.

In order to find the final equilibrium state of the system at a given  $P$ - $T$  condition, various potential valence and spin states and site occupancies of iron in Pv and Fp phases have been considered in our calculations, as well as two methods of treating the oxygen availability (oxygen fugacity). Specifically, we have considered an

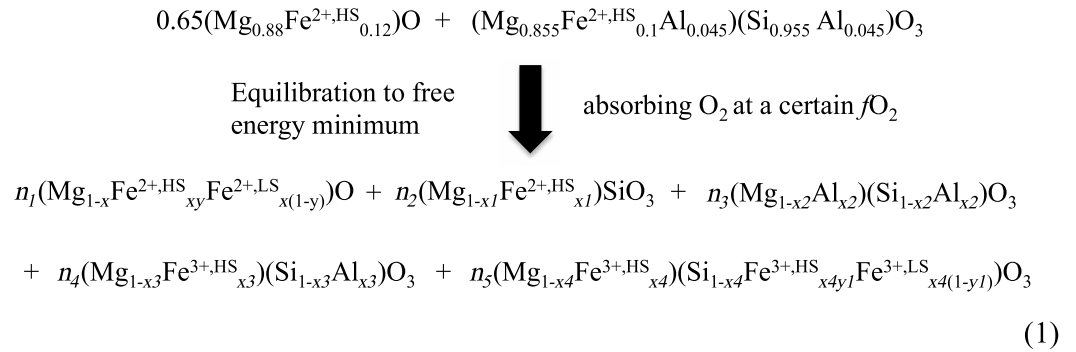


oxidation reaction model (equation (1)) and a chg. disp. reaction model (equation (2)) in our thermodynamic modeling. Variations in the oxygen fugacity ( $fO_2$ ) are also considered in the oxidation reaction model. Consideration of these different reactions helps us to understand both laboratory experimental results and behavior in the deep mantle, which can have significantly different  $fO_2$  values.

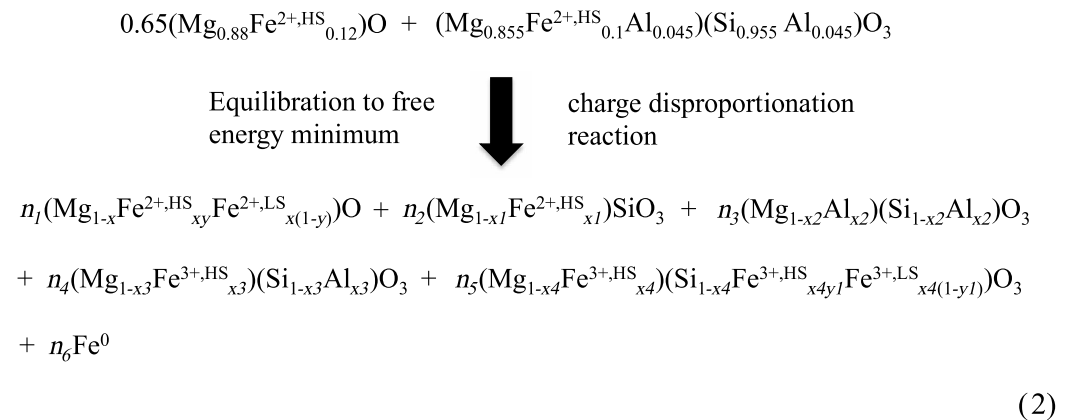
The oxidation reaction model is appropriate for modeling laboratory experiments. In the laboratory, the data were typically derived from chemical analyses of quenched samples originally equilibrated at high temperatures in systems with capsules that effectively buffer the  $fO_2$ . Depending on the type of the capsule used (e.g., metal, MgO, and diamond) and potentially the kinetics in the experiment, the  $fO_2$  of the system can vary significantly, making the interpretation of experimental results more difficult [Campbell *et al.*, 2009; Frost *et al.*, 2004; Irifune *et al.*, 2010; Lauterbach *et al.*, 2000; Nakajima *et al.*, 2012; Xu *et al.*, 2015]. Under equilibrium with the  $fO_2$  set by capsules used in most experimental conditions, metallic Fe cannot form, as it will be oxidized, and there is excess oxygen available to oxidize  $Fe^{2+}$  to  $Fe^{3+}$  [Xu *et al.*, 2015]. This explains why we do not have metallic Fe ( $Fe^0$ ) in the oxidation model as shown in the equation (1). In contrast, it is believed that there is no excess oxygen available in the lower mantle, and any  $Fe^{3+}$  that forms is created by the chg. disp. reaction ( $3Fe^{2+} \rightarrow 2Fe^{3+} + Fe^0$ ) [Frost *et al.*, 2004; McCammon, 1997; Xu *et al.*, 2015].

The chg. disp. reaction model is appropriate for modeling lower mantle relevant conditions. In this model, we have assumed that the lower mantle is not chemically reacting with the surrounding layers of the upper mantle and the outer core such that there is neither external free oxygen gas nor any significant amount of other oxidizing agents to oxidize  $Fe^{2+}$  available. In such a scenario, the only possible mechanism to produce  $Fe^{3+}$  is via the chg. disp. reaction.

In the oxidation reaction modeling we consider the following equilibration from our initial state.



In the chg. disp. reaction modeling we consider the following equilibration from our initial state.



For the oxidation reaction model, the grand potential of the system is minimized as a function of  $P$ ,  $T$ , and the chemical potential of oxygen  $\mu(O_2)$  such that the system is open to free  $O_2$ . For the charge disproportionation reaction model, the Gibbs energy is minimized as a function of  $P$ - $T$  such that the system is closed with respect to oxygen composition.

Equations (3) and (4) detail the phases and sublattice mixtures in a compact form for both models, while equations (5) and (6) express the total thermodynamic potentials of the system. Equation (5) represents the expression of the grand potential, which is minimized for the oxidation reaction model, where  $\Delta n$  is the amount of the absorbed  $O_2$ . This expression makes use of the expression for the grand potential ( $\Omega$ ) as  $\Omega = G(Pv + Fp) - \Delta n \times \mu(O_2)$  where  $G(Pv + Fp)$  is the total Gibbs energy of the solid phases, Pv and Fp. Equation (S6) is the expression of the Gibbs energy, which is minimized for the chg. disp. reaction model.

We use an ideal solution model to formulate the Gibbs and grand potential energies in equations (5) and (6), which treats the  $Mg^{2+}$ ,  $Si^{4+}$ ,  $Al^{3+}$ ,  $(Fe^{2+,HS})_{Fp}$ ,  $(Fe^{2+,LS})_{Fp}$ ,  $(Fe^{2+,HS})_{Pv}$ ,  $(Fe^{3+,HS,A-site})_{Pv}$ ,  $(Fe^{3+,HS,B-site})_{Pv}$ , and  $(Fe^{3+,LS,B-site})_{Pv}$  species as noninteracting species on each relevant sublattice. We have also checked the nonideality effect and find that it does not have any qualitative impact on the result of our ideal solution model (the details are discussed in SI section 1.2 [Blum and Zunger, 2004]). If one considers these effects, quantitative changes are  $<0.09$  for the Fe partitioning coefficient and  $<0.01$  for the  $Fe^{3+}/\Sigma Fe$  in Pv (the relative content of  $Fe^{3+}$  in Pv) at all the lower mantle relevant  $P$ - $T$  conditions. There is also no change for the Pv B-site occupancy. We thus did not consider the nonideality effect further in our model. In the ideal solution approximation, the mixture enthalpies ( $H$ ) can be written as a linear combination of their end-member values. The enthalpy of the end-members in the system was obtained DFT calculations. The configurational entropy ( $S_{config}$ ) and electronic-magnetic entropy of different Fe states ( $S_{mag}$ ) are modeled in the ideal noninteracting system following the approaches in Tsuchiya *et al.* [2006] and Xu *et al.* [2015]. The only additional terms required in the present model versus the previous reference [Xu *et al.*, 2015] are those in the configurational entropy for systems containing Al. These are treated in the standard way for a multicomponent ideal solution sublattice [Chang and Oates, 2009], e.g., as illustrated in equation (7) for the configurational entropy  $S_{config}(Pv, B-site)$  of the B-sublattice in Pv.

With the exception of a special situation for oxygen described next, no vibrational contributions to the free energies are included, as they are assumed to vary slightly between the different possible solid states of the system. The calculation of the vibrational effect is shown in SI section 1.3 [Anderson, 1989; Hsu *et al.*, 2010b; Sha and Cohen, 2010]. Similar to the nonideality effect, the inclusion of the vibrational effect does not have a significantly qualitative impact on our results. The quantitative changes are  $<0.1$  for the Fe partitioning coefficient and  $<0.05$  for the  $Fe^{3+}/\Sigma Fe$  in Pv at all the lower mantle relevant  $P$ - $T$  conditions. There is also no observable change for the Pv B-site occupancy. Therefore, the vibrational effect is not further considered in our model. The one exception to this approach is in the oxidation reaction model, where  $O_2$  can be absorbed into the system from the gas phase. In this case the vibrational contributions of oxygen atoms are present in the gas phase model and therefore should not be ignored in the ionic solid phase. Therefore, in our thermodynamic model we include an approximate solid phase vibrational free energy for oxygen, which is described in SI section 4.1 [Lee *et al.*, 2009; Yagi *et al.*, 1978].

The  $fO_2$  in different capsules as a function of  $P$ - $T$  and the calculation of the effective chemical potential of  $O_2$  can be found in the work of Xu *et al.* [2015] (section) 2.1.1 and SI section 1 for details). Using the expressions in S5 and S6 for the thermodynamic potentials of the system, we have then minimized these potentials to reach thermodynamic equilibrium conditions at any given conditions of the possible variables. More specifically, for the chg. disp. model, in order to find stable mineral phases with equilibrium iron content and spin/valence states, the Gibbs energy,  $G_{total}[Chg. Disp.]$ , is minimized with respect to  $(n_1:n_6, x, x_1:x_4, y, y_1)$  at each given  $P$ - $T$  condition. A corresponding minimization is also done for  $\Omega_{total}[Oxidation]$ .

$$\text{System}_{Oxidation} = (n_2 + n_3 + n_4 + n_5) \left( \frac{Mg_{n_2+n_3+n_4+n_5-x_2n_3-x_1n_2-x_3n_4-x_4n_5}}{n_2+n_3+n_4+n_5} Fe^{2+} \frac{x_1n_2}{n_2+n_3+n_4+n_5} Fe^{3+,HS} \frac{x_3n_4+x_4n_5}{n_2+n_3+n_4+n_5} Al^{3+} \frac{x_2n_3}{n_2+n_3+n_4+n_5} \right) \\ \left( \frac{Si_{n_2+n_3+n_4+n_5-x_2n_3-x_3n_4-x_4n_5}}{n_2+n_3+n_4+n_5} Fe^{3+,HS} \frac{x_4n_5y_1}{n_2+n_3+n_4+n_5} Fe^{3+,LS} \frac{x_4n_5(1-y_1)}{n_2+n_3+n_4+n_5} Al^{3+} \frac{x_2n_3+x_3n_4}{n_2+n_3+n_4+n_5} \right) O_3 + n_1 (Mg_{1-x} Fe_{xy}^{2+,HS} Fe_{x(1-y)}^{2+,LS}) O \quad (3)$$

$$\text{System}_{ChgDisp} = \text{System}_{Oxidation} + n_6 Fe^0 \quad (4)$$

$$\Omega_{total}[Oxidation] = \{ G_{total}[ChgDisp] - n_6 H[Fe^0] + n_6 TS(Fe^0) \} - \Delta n \mu(O_2) \quad (5)$$

$$\begin{aligned}
G_{\text{total}}[\text{ChgDisp}] = & n_1 y H[(\text{Mg}_{1-x} \text{Fe}_x^{2+, \text{HS}}) \text{O}] + n_1 (1-y) H[(\text{Mg}_{1-x} \text{Fe}_x^{2+, \text{LS}}) \text{O}] + n_2 H[(\text{Mg}_{1-x_1} \text{Fe}_{x_1}^{2+, \text{HS}}) \text{SiO}_3] \\
& + n_3 H[(\text{Mg}_{1-x_2} \text{Al}_{x_2}^{3+}) (\text{Si}_{1-x_2} \text{Al}_{x_2}^{3+}) \text{O}_3] + n_4 H[(\text{Mg}_{1-x_3} \text{Fe}_{x_3}^{3+, \text{HS}}) (\text{Si}_{1-x_3} \text{Al}_{x_3}^{3+}) \text{O}_3] \\
& + n_5 y_1 H[(\text{Mg}_{1-x_4} \text{Fe}_{x_4}^{3+, \text{HS}}) (\text{Si}_{1-x_4} \text{Fe}_{x_4}^{3+, \text{HS}}) \text{O}_3] + n_5 (1-y_1) H[(\text{Mg}_{1-x_4} \text{Fe}_{x_4}^{3+, \text{HS}}) (\text{Si}_{1-x_4} \text{Fe}_{x_4}^{3+, \text{LS}}) \text{O}_3] \\
& + n_6 H[\text{Fe}^0] - n_1 x y T S_{\text{mag}}(\text{Fe}^{2+, \text{HS}}, \text{Fp}) - n_1 x (1-y) T S_{\text{mag}}(\text{Fe}^{2+, \text{LS}}, \text{Fp}) - \\
& n_2 x_1 T S_{\text{mag}}(\text{Fe}^{2+, \text{HS}}, \text{Pv, A-site}) - (n_4 x_3 + n_5 x_4) T S_{\text{mag}}(\text{Fe}^{2+, \text{HS}}, \text{Pv, A-site}) - \\
& n_5 x_4 y_1 T S_{\text{mag}}(\text{Fe}^{3+, \text{HS}}, \text{Pv, B-site}) - n_5 x_4 (1-y_1) T S_{\text{mag}}(\text{Fe}^{3+, \text{LS}}, \text{Pv, B-site}) - n_6 T S(\text{Fe}^0) \\
& - (n_2 + n_3 + n_4 + n_5) T S_{\text{config}}(\text{Pv, A-site}) - (n_2 + n_3 + n_4 + n_5) T S_{\text{config}}(\text{Pv, B-site}) \\
& - n_1 T S_{\text{config}}(\text{Fp, A-site})
\end{aligned} \tag{6}$$

$$S_{\text{config}}(\text{Pv, B-site}) = -k_B (X_{\text{Si}} \ln X_{\text{Si}} + X_{\text{Fe}, 3+, \text{HS}} \ln X_{\text{Fe}, 3+, \text{HS}} + X_{\text{Fe}, 3+, \text{LS}} \ln X_{\text{Fe}, 3+, \text{LS}} + X_{\text{Al}, 3+} \ln X_{\text{Al}, 3+}) \tag{7}$$

The mechanism for creating oxygen vacancies is not specifically considered in our modeling here as the oxygen vacancies have been predicted to be a very high energy defect (see our previous work [Xu *et al.*, 2015] for details).

### 4.3. Parameters for the DFT Calculations

Our ab initio calculations are performed using the Vienna ab initio simulation package (VASP) based on DFT. The projector-augmented wave (PAW) method [Blochl, 1994] is used for the effective potentials of all the atoms in the system. The PAW potentials we used included valence electrons  $2p^6 3s^2$  for Mg,  $3s^2 3p^2$  for Si,  $2s^2 2p^4$  for O,  $3p^6 3d^7 4s^1$  for Fe, and  $3s^2 3p^1$  for Al. A cutoff energy of 600 eV is used to ensure that the plane wave basis is large enough for the calculations to converge.

It is well known that the normal Local Density Approximation (LDA) and Generalized Gradient Approximation (GGA) functionals often provide inaccurate energetics for transition metal oxides, including oxides containing Fe [Wang *et al.*, 2006]. All the calculations in this work are therefore performed with HSE06 hybrid functional [Heyd *et al.*, 2003; Paier *et al.*, 2006] as implemented in the VASP code. The fraction of the exact Hartree-Fock exchange functional is set to be 0.25 (i.e., we set AEXX = 0.25 in the INCAR file). The HSE06 functional has been shown to yield significantly more accurate energetics for transition metal redox reactions than standard LDA or GGA techniques [Chevrier *et al.*, 2010]. All details concerning the  $k$  points and supercell setup information are shown in SI Table S3 [Dubrovinsky *et al.*, 2000]. The choices of the  $k$  point mesh yield a convergence of the total energy of a supercell within 1 meV/atom, while the structural relaxation is converged to less than  $10^{-3}$  eV in the total energy, yielding the average forces between atoms to be about 0.01 eV/Å. The validation of our ab initio calculations for these high-pressure phases in comparison with experimental equation of states (EOS) is shown in SI section 3.1 [Birch, 1986; Catalli *et al.*, 2011b; Catalli *et al.*, 2010; Dubrovinsky *et al.*, 2000; Fiquet *et al.*, 2000; Jacobsen *et al.*, 2002; Lin *et al.*, 2013, 2005; Lundin *et al.*, 2008; Mao *et al.*, 2011; Mathon *et al.*, 2004; Speziale *et al.*, 2001]. It should be noted here that among all the DFT calculated energies of the end-members in our thermodynamic model, two of them are obtained based on semiempirical approaches. The first one is the enthalpy of metallic Fe as a function of pressures, where the experimental EOS parameters are used. The other one is the enthalpy of LS Fp ( $\text{Mg, Fe}^{\text{LS}}\text{O}$ ) as a function of pressures, where a constant energy shift is applied to match with previous experimental and theoretical results of the spin transition region (please refer to SI section 3.1 for details [Lin *et al.*, 2013; Tsuchiya *et al.*, 2006]).

### 4.4. Density and Bulk Modulus of the Lower Mantle Phases

To calculate the density and bulk modulus of the lower mantle phases along an expected geotherm [Brown and Shankland, 1981], we have considered high-temperature effects on the volume and bulk modulus of the solid end-members in the system at high pressures. It should be noted here that the thermal expansion influence is not included in our Gibbs energy minimization calculation to find the equilibrium state of the system. After we get the different end-members contents in equilibrium, we consider the high-temperature effects on volume and bulk modulus to correct our corresponding DFT values  $V(P)^{\text{DFT}}$ , isothermal  $K_T(P)^{\text{DFT}}$ . Then we calculate the adiabatic bulk modulus  $K_S$  for the bulk sound velocity calculation. After we obtain the density and the adiabatic bulk modulus of each lower mantle phase, the Voigt-Reuss-Hill average is used to calculate the bulk modulus of the lower mantle [Lu *et al.*, 2013; Murakami *et al.*, 2012]. Please refer to

the SI section 4.2 for the calculation details of the lower mantle density, bulk modulus, and bulk sound velocity.

# Acknowledgments

D. Morgan and S. Xu acknowledge financial support from the United States National Science Foundation (EAR-0968685). J.F. Lin acknowledges financial support from the United States National Science Foundation (EAR-1446946). Computations in this work benefitted from the use of the Extreme Science and Engineering Discovery Environment (XSEDE), which is supported by National Science Foundation grant OCI-1053575. The authors appreciate all the previous works cited in the supporting information. The data shown in the figures and the tables are available by contacting the corresponding author (D. Morgan: ddmorgan@wisc.edu) upon request.

# References

- Ammann, M. W., J. P. Brodholt, J. Wookey, and D. P. Dobson (2010), First-principles constraints on diffusion in lower-mantle minerals and a weak D'' layer, *Nature*, 465(7297), 462–465, doi:10.1038/nature09052.
- Anderson, D. L. (1989), *Theory of the Earth*, Blackwell Sci. Publ., Boston, Mass.
- Auzende, A., J. Badro, F. J. Ryerson, P. K. Weber, S. J. Fallon, A. Addad, J. Siebert, and G. Fiquet (2008), Element partitioning between magnesium silicate perovskite and ferropericlase: New insights into bulk lower-mantle geochemistry, *Earth Planet. Sci. Lett.*, 269, 164–174.
- Badro, J., G. Fiquet, F. Guyot, J. P. Rueff, V. V. Struzhkin, G. Vanko, and G. Monaco (2003), Iron partitioning in Earth's mantle: Toward a deep lower mantle discontinuity, *Science*, 300(5620), 789–791, doi:10.1126/science.1081311.
- Bengtson, A., K. Persson, and D. Morgan (2008), Ab initio study of the composition dependence of the pressure-induced spin crossover in perovskite ( $\text{Mg}_{1-x}\text{Fe}_x\text{SiO}_3$ ), *Earth Planet. Sci. Lett.*, 265(3–4), 535–545, doi:10.1016/j.epsl.2007.10.049.
- Birch, F. (1986), Equation of state and thermodynamic parameters of NaCl to 300 kbar in the high-temperature domain, *J. Geophys. Res.*, 91, 4949–4954, doi:10.1029/JB091iB05p04949.
- Bloch, P. E. (1994), Projector augmented-wave method, *Phys. Rev. B*, 50(24), 17,953–17,979, doi:10.1103/PhysRevB.50.17953.
- Blum, V., and A. Zunger (2004), Mixed-basis cluster expansion for thermodynamics of bcc alloys, *Phys. Rev. B*, 70, 155108, doi:10.1103/PhysRevB.70.155108.
- Brodholt, J. P. (2000), Pressure-induced changes in the compression mechanism of aluminous perovskite in the Earth's mantle, *Nature*, 407, 620–622.
- Brown, J. M., and T. J. Shankland (1981), Thermodynamic parameters in the Earth as determined from seismic profiles, *Geophys. J. R. Astron. Soc.*, 66, 579–596.
- Cammarano, F., H. Marquardt, S. Speziale, and P. J. Tackley (2010), Role of iron-spin transition in ferropericlase on seismic interpretation: A broad thermochemical transition in the mid mantle?, *Geophys. Res. Lett.*, 37, L03308, doi:10.1029/2009GL041583.
- Campbell, A. J., L. Danielson, K. Richter, C. T. Seagle, Y. Wang, and V. B. Prakapenka (2009), High pressure effects on the iron–iron oxide and nickel–nickel oxide oxygen fugacity buffers, *Earth Planet. Sci. Lett.*, 286(3–4), 556–564, doi:10.1016/j.epsl.2009.07.022.
- Catali, K., S. H. Shim, V. B. Prakapenka, J. Zhao, W. Sturhahn, P. Chow, Y. Xiao, H. Liu, H. Cynn, and W. J. Evans (2010), Spin state of ferric iron in  $\text{MgSiO}_3$  perovskite and its effect on elastic properties, *Earth Planet. Sci. Lett.*, 289(1–2), 68–75, doi:10.1016/j.epsl.2009.10.029.
- Catali, K., S. H. Shim, P. Dera, V. B. Prakapenka, J. Zhao, W. Sturhahn, P. Chow, Y. Xiao, H. Cynn, and W. J. Evans (2011a), Effects of the  $\text{Fe}^{3+}$  spin transition on the properties of aluminous perovskite—New insights for lower-mantle seismic heterogeneities, *Earth Planet. Sci. Lett.*, 310(3–4), 293–302, doi:10.1016/j.epsl.2011.08.018.
- Catali, K., S. H. Shim, P. Dera, V. B. Prakapenka, J. Zhao, W. Sturhahn, P. Chow, Y. Xiao, H. Cynn, and W. J. Evans (2011b), Effects of the  $\text{Fe}^{3+}$  spin transition on the properties of aluminous perovskite—New insights for lower-mantle seismic heterogeneities, *Earth Planet. Sci. Lett.*, 310, 293–302.
- Chang, Y. A., and W. A. Oates (2009), *Materials Thermodynamics*, John Wiley, Hoboken, N. J.
- Chevrier, V. L., S. P. Ong, R. Armiento, M. K. Y. Chan, and G. Ceder (2010), Hybrid density functional calculations of redox potentials and formation energies of transition metal compounds, *Phys. Rev. B*, 82(7), doi:10.1103/PhysRevB.82.075122.
- Crowhurst, J. C., J. M. Brown, A. F. Goncharov, and S. D. Jacobsen (2008), Elasticity of (Mg,Fe)O through the spin transition of iron in the lower mantle, *Science*, 319, 451–453.
- Dubrovinsky, L., S. Saxena, F. Tutti, S. Rekhi, and T. LeBehan (2000), In situ X-ray study of thermal expansion and phase transition of iron at multimegabar pressure, *Phys. Rev. Lett.*, 84, 1720–1723.
- Dziewonski, A. M., and D. L. Anderson (1981), Preliminary reference Earth model, *Phys. Earth Planet. Inter.*, 25, 297–356.
- Fiquet, G., A. Dewaele, D. Andraut, M. Kunz, and T. Le Bihan (2000), Thermoelastic properties and crystal structure of  $\text{MgSiO}_3$  perovskite at lower mantle pressure and temperature conditions, *Geophys. Res. Lett.*, 27(1), 21–24, doi:10.1029/1999GL008397.
- Frost, D. J., C. Liebske, F. Langenhorst, C. A. McCammon, R. Tronnes, and D. C. Rubie (2004), Experimental evidence for the existence of iron-rich metal in the Earth's lower mantle, *Nature*, 428, 409–412.
- Fukai, Y., and T. Suzuki (1986), Iron–water interaction under high pressure and its implication in the evolution of the Earth, *J. Geophys. Res.*, 91, 9222–9230, doi:10.1029/JB091iB09p09222.
- Goncharov, A. F., V. V. Struzhkin, and S. D. Jacobsen (2006), Reduced radiative conductivity of low-spin (Mg,Fe)O in the lower mantle, *Science*, 312, 1205–1207.
- Grocholski, B., S. H. Shim, W. Sturhahn, J. Zhao, Y. Xiao, and P. C. Chow (2009), Spin and valence states of iron in  $(\text{Mg}_{0.8}\text{Fe}_{0.2})\text{SiO}_3$  perovskite, *Geophys. Res. Lett.*, 36, L24303, doi:10.1029/2009GL041262.
- Halliday, A. N., and D. C. Lee (1999), Tungsten isotopes and the early development of the Earth and Moon, *Geochem. Cosmochem. Acta*, 63, 4157–4179.
- Heyd, J., G. E. Scuseria, and M. Ernzerhof (2003), Hybrid functionals based on a screened Coulomb potential, *J. Chem. Phys.*, 118(18), 8207, doi:10.1063/1.1564060.
- Hsu, H., K. Umamoto, P. Blaha, and R. M. Wentzcovitch (2010a), Spin states and hyperfine interactions of iron in (Mg,Fe) $\text{SiO}_3$  perovskite under pressure, *Earth Planet. Sci. Lett.*, 294(1–2), 19–26, doi:10.1016/j.epsl.2010.02.031.
- Hsu, H., K. Umamoto, Z. Wu, and R. M. Wentzcovitch (2010b), Spin-state crossover of iron in lower-mantle minerals: Results of DFT + U investigations, *Rev. Mineral. Geochem.*, 71, 169–199.
- Hsu, H., P. Blaha, M. Cococcioni, and R. M. Wentzcovitch (2011), Spin-state crossover and hyperfine interactions of ferric iron in  $\text{MgSiO}_3$  perovskite, *Phys. Rev. Lett.*, 106, 1–4.
- Hsu, H., Y. G. Yu, and R. M. Wentzcovitch (2012), Spin crossover of iron in aluminous  $\text{MgSiO}_3$  perovskite and post-perovskite, *Earth Planet. Sci. Lett.*, 359–360, 34–39.
- Irfune, T. (1994), Absence of an aluminous phase in the upper part of the Earth's lower mantle, *Nature*, 370, 131–133.
- Irfune, T., T. Shinmei, C. A. McCammon, N. Miyajima, D. C. Rubie, and D. J. Frost (2010), Iron partitioning and density changes of pyrolite in Earth's lower mantle, *Science*, 327(8), 193–195, doi:10.1126/science.1181443.
- Jackson, J. M., W. Sturhahn, G. Shen, J. Zhao, M. Y. Hu, D. Errandonea, J. D. Bass, and Y. Fei (2005), A synchrotron Mössbauer spectroscopy study of (Mg,Fe) $\text{SiO}_3$  perovskite up to 120 GPa, *Am. Mineral.*, 90, 199–205.

- Jacobsen, S. D., H. J. Reichmann, H. A. Spetzler, S. J. Mackwell, J. R. Smyth, R. J. Angel, and C. A. McCammon (2002), Structure and elasticity of single-crystal (Mg,Fe)O and a new method of generating shear waves for gigahertz ultrasonic interferometry, *J. Geophys. Res.*, *107*(B2), 2037, doi:10.1029/2001JB000490.
- Kesson, S. E., J. D. Fitz Gerald, and J. M. Shelley (1998), Mineralogy and dynamics of a pyrolite lower mantle, *Nature*, *393*, 252–255.
- Kobayashi, Y., T. Kondo, E. Ohtani, N. Hirao, N. Miyajima, T. Yagi, T. Nagase, and T. Kikegawa (2005), Fe-Mg partitioning between (Mg, Fe)SiO<sub>3</sub> post-perovskite, perovskite, and magnesiowüstite in the Earth's lower mantle, *Geophys. Res. Lett.*, *32*, L19301, doi:10.1029/2005GL023257.
- Lauterbach, S., C. McCammon, P. Van Aken, F. Langenhorst, and F. Seifert (2000), Mossbauer and ELNES spectroscopy of (Mg,Fe)(Si,Al)O<sub>3</sub> perovskite: A highly oxidised component of the lower mantle, *Contrib. Mineral. Petrol.*, *138*, 17–26.
- Lee, Y.-L., J. Kleis, J. Rossmeisl, and D. Morgan (2009), Ab initio energetics of LaBO<sub>3</sub>(001) (*B* = Mn, Fe, Co, and Ni) for solid oxide fuel cell cathodes, *Phys. Rev. B*, *80*(22), doi:10.1103/PhysRevB.80.224101.
- Lin, J. F., V. V. Struzhkin, S. D. Jacobsen, M. Y. Hu, P. Chow, J. Kung, H. Liu, H. K. Mao, and R. J. Hemley (2005), Spin transition of iron in magnesiowüstite in the Earth's lower mantle, *Nature*, *436*(7049), 377–380, doi:10.1038/nature03825.
- Lin, J. F., E. E. Alp, Z. Mao, T. Inoue, C. McCammon, Y. Xiao, P. Chow, and J. Zhao (2012), Electronic spin states of ferric and ferrous iron in the lower-mantle silicate perovskite, *Am. Mineral.*, *97*, 592–597.
- Lin, J. F., S. Speziale, Z. Mao, and H. Marquardt (2013), Implications for deep mantle geophysics and geochemistry, *Rev. Geophys.*, *51*, 244–270, doi:10.1002/rog.20010.
- Lu, C., Z. Mao, J. F. Lin, K. K. Zhuravlev, S. N. Tkachev, and V. B. Prakapenka (2013), Elasticity of single-crystal iron-bearing pyrope up to 20 GPa and 750 K, *Earth Planet. Sci. Lett.*, *361*, 134–142.
- Lundin, S., K. Catalli, J. Santillán, S.-H. Shim, V. B. Prakapenka, M. Kunz, and Y. Meng (2008), Effect of Fe on the equation of state of mantle silicate perovskite over 1Mbar, *Phys. Earth Planet. Inter.*, *168*, 97–102.
- Mao, Z., J.-F. Lin, J. Liu, and V. B. Prakapenka (2011), Thermal equation of state of lower-mantle ferropericlase across the spin crossover, *Geophys. Res. Lett.*, *38*, L23308, doi:10.1029/2011GL049915.
- Marquardt, H., S. Speziale, H. J. Reichmann, D. J. Frost, and F. R. Schilling (2009), Single-crystal elasticity of (Mg<sub>0.9</sub>Fe<sub>0.1</sub>)O to 81 GPa, *Earth Planet. Sci. Lett.*, *287*, 345–352.
- Mathon, O., F. Baudelet, J. Itié, A. Polian, M. d'Astuto, J. Chervin, and S. Pascarelli (2004), Dynamics of the magnetic and structural  $\alpha$ - $\epsilon$  phase transition in iron, *Phys. Rev. Lett.*, *93*(25), doi:10.1103/PhysRevLett.93.255503.
- McCammon, C. A. (1997), Perovskite as a possible sink for ferric iron in the lower mantle, *Nature*, *387*, 694–696.
- Muir, J. M. R., and J. P. Brodholt (2016), Ferrous iron partitioning in the lower mantle, *Phys. Earth Planet. Inter.*, *257*, 12–17.
- Murakami, M., K. Hirose, N. Sata, and Y. Ohishi (2005), Post-perovskite phase transition and mineral chemistry in the pyrolytic lowermost mantle, *Geophys. Res. Lett.*, *32*, L03304, doi:10.1029/2004GL021956.
- Murakami, M., Y. Ohishi, N. Hirao, and K. Hirose (2012), A perovskitic lower mantle inferred from high-pressure, high-temperature sound velocity data, *Nature*, *485*, 90–94.
- Nakajima, Y., D. J. Frost, and D. C. Rubie (2012), Ferrous iron partitioning between magnesium silicate perovskite and ferropericlase and the composition of perovskite in the Earth's lower mantle, *J. Geophys. Res.*, *117*, B08201, doi:10.1029/2012JB009151.
- Paier, J., M. Marsman, K. Hummer, G. Kresse, I. C. Gerber, and J. G. Ángyán (2006), Screened hybrid density functionals applied to solids, *J. Chem. Phys.*, *125*(24), 249901, doi:10.1063/1.2403866.
- Persson, K., A. Bengtson, G. Ceder, and D. Morgan (2006), Ab initio study of the composition dependence of the pressure-induced spin transition in the (Mg<sub>1-x</sub>Fe<sub>x</sub>)O system, *Geophys. Res. Lett.*, *33*, L16306, doi:10.1029/2006GL026621.
- Pownceby, M. I., and H. S. C. O'Neil (1994), Thermodynamic data from redox reactions at high temperatures: IV. Calibration of the Re-ReO<sub>2</sub> oxygen buffer from EMF and NiO plus Ni-Pd redox sensor measurements, *Contrib. Mineral. Petrol.*, *118*, 130–137.
- Prescher, C., F. Langenhorst, L. Dubrovinsky, V. Prakapenka, and N. Miyajima (2014), The effect of Fe spin crossovers on its partitioning behavior and oxidation state in a pyrolytic Earth's lower mantle system, *Earth Planet. Sci. Lett.*, *399*, 86–91.
- Riccolleau, A., J. P. Perrillat, G. Fiquet, I. Daniel, J. Matas, A. Addad, N. Menguy, H. Cardon, M. Mezouar, and N. Guignot (2010), Phase relations and equation of state of a natural MORB: Implications for the density profile of subducted oceanic crust in the Earth's lower mantle, *J. Geophys. Res.*, *115*, B08202, doi:10.1029/2009JB006709.
- Ringwood, A. E. (1966), The chemical composition and origin of the Earth, *Adv. Earth Sci.*, *287*–356.
- Sakai, T., E. Ohtani, H. Terasaki, N. Sawada, Y. Kobayashi, M. Miyahara, M. Nishijima, N. Hirao, Y. Ohishi, and T. Kikegawa (2009), Fe-Mg partitioning between perovskite and ferropericlase in the lower mantle, *Am. Mineral.*, *94*, 921–925.
- Sha, X., and R. E. Cohen (2010), First-principles thermal equation of state and thermoelasticity of hcp Fe at high pressures, *Phys. Rev. B*, *81*(9), doi:10.1103/PhysRevB.81.094105.
- Shukla, G., Z. Wu, H. Hsu, A. Floris, M. Cococcioni, and R. Wentzcovitch (2015), Thermoelasticity of Fe<sup>2+</sup>-bearing bridgmanite, *Geophys. Res. Lett.*, *42*, 1741–1749, doi:10.1002/2014GL062888.
- Sinmyo, R., and K. Hirose (2013), Iron partitioning in pyrolytic lower mantle, *Phys. Chem. Miner.*, *40*(2), 107–113, doi:10.1007/s00269-012-0551-7.
- Sinmyo, R., K. Hirose, D. Nishio-Hamane, Y. Seto, K. Fujino, N. Sata, and Y. Ohishi (2008a), Partitioning of iron between perovskite/postperovskite and ferropericlase in the lower mantle, *J. Geophys. Res.*, *113*, B11204, doi:10.1029/2008JB005730.
- Sinmyo, R., H. Ozawa, K. Hirose, A. Yasuhara, N. Endo, N. Sata, and Y. Ohishi (2008b), Ferric iron content in (Mg,Fe)SiO<sub>3</sub> perovskite and post-perovskite at deep lower mantle conditions, *Am. Mineral.*, *93*, 1899–1902.
- Speziale, S., C.-S. Zha, T. S. Duffy, R. J. Hemley, and H.-k. Mao (2001), Quasi-hydrostatic compression of magnesium oxide to 52 GPa: Implications for the pressure-volume-temperature equation of state, *J. Geophys. Res.*, *106*(B1), 515–528, doi:10.1029/2000JB900318.
- Stackhouse, S., J. P. Brodholt, and G. D. Price (2007), Electronic spin transitions in iron-bearing MgSiO<sub>3</sub> perovskite, *Earth Planet. Sci. Lett.*, *253*, 282–290.
- Stagno, V., and D. J. Frost (2010), Carbon speciation in the asthenosphere: Experimental measurements of the redox conditions at which carbonate-bearing melts coexist with graphite or diamond in peridotite assemblages, *Earth Planet. Sci. Lett.*, *300*(1–2), 72–84, doi:10.1016/j.epsl.2010.09.038.
- Stagno, V., D. J. Frost, C. McCammon, H. Mohseni, and Y. Fei (2015), The oxygen fugacity at which graphite or diamond forms from carbonate-bearing melts in eclogitic rocks, *Contrib. Mineral. Petrol.*, *169*(2), 16.
- Sturhahn, W., J. M. Jackson, and J. F. Lin (2005), The spin state of iron in minerals of Earth's lower mantle, *Geophys. Res. Lett.*, *32*, L12307, doi:10.1029/2005GL022802.
- Tange, Y., Y. Nishihara, and T. Tsuchiya (2009), Unified analyses for P-V-T equation of state of MgO: A solution for pressure-scale problems in high P-T experiments, *J. Geophys. Res.*, *114*, B03208, doi:10.1029/2008JB005813.
- Tange, Y., Y. Kuwayama, T. Irifune, K.-i. Funakoshi, and Y. Ohishi (2012), P-V-T equation of state of MgSiO<sub>3</sub> perovskite based on the MgO pressure scale: A comprehensive reference for mineralogy of the lower mantle, *J. Geophys. Res.*, *117*, B06201, doi:10.1029/2011JB008988.

- Tsuchiya, T., R. Wentzcovitch, C. da Silva, and S. de Gironcoli (2006), Spin transition in magnesiowüstite in Earth's lower mantle, *Phys. Rev. Lett.*, *96*(19), doi:10.1103/PhysRevLett.96.198501.
- van Westrenen, W., et al. (2005), Thermoelastic properties of  $(\text{Mg}_{0.64}\text{Fe}_{0.36})\text{O}$  ferropericlase based on in situ X-ray diffraction to 26.7 GPa and 2173K, *Phys. Earth Planet. Inter.*, *151*, 163–176.
- Vilella, K., S. H. Shim, C. G. Farnetani, and J. Badro (2015), Spin state transition and partitioning of iron: Effects on mantle dynamics, *Earth Planet. Sci. Lett.*, *417*, 57–66.
- Wang, L., T. Maxisch, and G. Ceder (2006), Oxidation energies of transition metal oxides within the GGA + U framework, *Phys. Rev. B*, *73*(19), doi:10.1103/PhysRevB.73.195107.
- Wang, X., T. Tsuchiya, and A. Hase (2015), Computational support for a pyrolitic lower mantle containing ferric iron, *Nat. Geosci.*, doi:10.1038/ngeo2458.
- Wood, B. J. (2000), Phase transformations and partitioning relations in peridotite under lower mantle conditions, *Earth Planet. Sci. Lett.*, *174*, 341–354.
- Wu, Z., and R. M. Wentzcovitch (2014), Spin crossover in ferropericlase and velocity heterogeneities in the lower mantle, *Proc. Natl. Acad. Sci. U. S. A.*, *111*, 10,468–10,472.
- Xu, S., S. H. Shim, and D. Morgan (2015), Origin of  $\text{Fe}^{3+}$  in Fe-containing, Al-free mantle silicate perovskite, *Earth Planet. Sci. Lett.*, *409*, 319–328.
- Yagi, T., H. K. Mao, and P. M. Bell (1978), Structure and crystal chemistry of perovskite-type  $\text{MgSiO}_3$ , *Phys. Chem. Miner.*, *3*, 97–110.
- Zhang, F. W., and A. R. Oganov (2006), Valence state and spin transitions of iron in Earth's mantle silicates, *Earth Planet. Sci. Lett.*, *249*, 436–443.